Journal of Applied Physics

Origin of enhanced piezoelectric properties revealed through electric field driven studies in $0.94(Na_{0.5}Bi_{0.5}TiO_3)-0.06(Ba_{0.85}Ca_{0.15}Ti_{0.9}Zr_{0.1}$ ceramics

Cite as: J. Appl. Phys. **127**, 134102 (2020); https://doi.org/10.1063/1.5136293
Submitted: 14 November 2019 . Accepted: 12 March 2020 . Published Online: 01 April 2020

Karthik T, Sudhindra Rayaprol, Vasudeva Siruguri, and Saket Asthana

View Online Export Citation CrossMark

ARTICLES YOU MAY BE INTERESTED IN

The effect of A-site cation on ferroelectric properties in $Na_{0.5}Bi_{0.5}TiO_3$-based materials: Correlation between Burns temperature and remanent polarization
Journal of Applied Physics **127**, 144102 (2020); https://doi.org/10.1063/1.5131201

Perovskite lead-free piezoelectric ceramics
Journal of Applied Physics **127**, 190901 (2020); https://doi.org/10.1063/5.0006261

$BaTiO_3$-based piezoelectrics: Fundamentals, current status, and perspectives
Applied Physics Reviews **4**, 041305 (2017); https://doi.org/10.1063/1.4990046

Challenge us.
What are your needs for periodic signal detection?
Watch

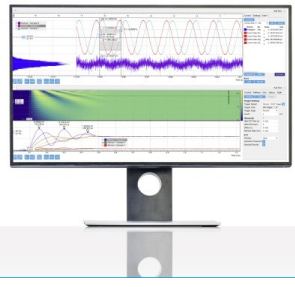

Zurich Instruments

© 2020 Author(s).

AIP Publishing

Journal of Applied Physics ARTICLE scitation.org/journal/jap

Origin of enhanced piezoelectric properties revealed through electric field driven studies in $0.94(Na_{0.5}Bi_{0.5}TiO_3)–0.06(Ba_{0.85}Ca_{0.15}Ti_{0.9}Zr_{0.1}O_3)$ ceramics

Cite as: J. Appl. Phys. **127**, 134102 (2020); doi: 10.1063/1.5136293
Submitted: 14 November 2019 · Accepted: 12 March 2020 ·
Published Online: 1 April 2020

View Online Export Citation CrossMark

Karthik T,[1,2,a)] Sudhindra Rayaprol,[3] Vasudeva Siruguri,[3] and Saket Asthana[1,a)]

AFFILIATIONS

[1]Advanced Functional Materials Laboratory, Department of Physics, Indian Institute of Technology Hyderabad, Hyderabad, Telangana 502285, India
[2]Centre for Materials for Electronics Technology, Thrissur 680581, Kerala, India
[3]UGC-DAE-Consortium for Scientific Research, Mumbai Centre, BARC Campus, Mumbai 400085, India

[a)]**Authors to whom correspondence should be addressed:** asthanas@iith.ac.in and karthik.t@cmet.gov.in

ABSTRACT

A single phase $0.94(Na_{0.5}Bi_{0.5}TiO_3)–0.06(Ba_{0.85}Ca_{0.15}Ti_{0.9}Zr_{0.1}O_3)$ solid solution (i.e., BCZT-0.06) is prepared using a conventional solid-state sintering route with enhanced piezo and ferroelectric properties as compared to $Na_{0.5}Bi_{0.5}TiO_3$ (NBT). In the context of understanding the origin of enhanced piezoelectric properties in a BCZT-0.06 specimen, electric field driven studies on different length scales, viz., global, local, and electronic structure, are carried out using x-ray/neutron diffraction, Raman scattering, and UV–Vis spectroscopic techniques. An analysis on different length scales of the electric field-driven BCZT-0.06 specimen displays minimum rhombohedral lattice distortion (δ_r), reduced homogeneous lattice strain (δ), octahedral strain (ζ), and pronounced Ti-cation displacement along the polar [111] direction as compared to parent NBT. The enhanced ferro and piezoelectric responses observed in the BCZT-0.06 specimen have been attributed to the ease of non-180° domain re-orientation, domain switching, and domain wall motion due to reduced strain coupled with a polarization extension mechanism.

Published under license by AIP Publishing. https://doi.org/10.1063/1.5136293

I. INTRODUCTION

Lead free piezoceramics have been extensively studied over the past 10 years, and among them, $Na_{0.5}Bi_{0.5}TiO_3$ (NBT)-based systems are found to be promising for applications such as actuators, transducers, ultrasonic motors, ultrasonic cleaners, energy harvesters, knock sensors, medical probes, etc.[1–4] It is known that for a polycrystalline ferroelectric ceramic to exhibit piezoelectricity at the macroscopic length scale, it must go through a poling process.[5] However, in most of the cases, the structure of a ferroelectric system is studied in the unpoled state and is correlated with the properties observed in the poled state. Thus, there is a possibility of mismatch in establishing a one-to-one structure property correlation. Several recent studies evidenced a noticeable variation in the structure of parent NBT over different length scales with the effect of an electric field. Based on the x-ray, synchrotron, and neutron diffraction (ND) measurements on poled NBT specimens, Rao and Ranjan showcased a pronounced rhombohedral distortion on a global scale.[6] Transmission electron microscopic (TEM) studies performed on the poled NBT specimens depict a drastic reduction in the coherence length of the localized in-phase tilt and strain heterogeneities, thereby enabling a complete *R3c* structural stabilization on a global scale upon poling.[7] In our recent study on NBT, we have evidenced a polarization extension mechanism through electric field driven structural analysis using x-ray and Raman scattering techniques.[8] In another recent study, we have directly evidenced the exact nature of polar ordering in NBT through electric field driven *in situ* high temperature polarization measurements.[9] Apart from parent NBT, the electric field also alters the phase stabilization in several NBT-based solid solution systems. Daniels *et al.*

Published under license by AIP Publishing.

observed that in 0.93NBT–0.07BT (BT: $BaTiO_3$) morphotrophic phase boundary (MPB) composition, the electric field alters the structure to a tetragonal phase from the R (rhombohedral) + T (tetragonal) phase co-existence in the unpoled state.[10] Picht *et al.* performed x-ray diffraction (XRD) studies at compositions at and around the MPB. They describe the co-existence of rhombohedral and tetragonal phases in the unpoled sample and found that the co-existence continues in the poled sample, but the nature of each phase changes quite dramatically.[11] Similarly, in NBT–KBT (KBT: $K_{0.5}Bi_{0.5}TiO_3$) MPB composition, Royles *et al.* showed an electric field-induced phase transition from the rhombohedral to the mixed phase of rhombohedral and tetragonal at an electric field $E \geq 2$ kV mm^{-1}.[12] Otoničar *et al.* observed field-induced structural changes from a general pseudocubic phase into the T and/or R structures for the MPB composition.[13] Ma *et al.* constructed a new MPB in the poled NBT–BT system through a novel method of electron diffraction analysis and provided the microstructural origin of previously unexplained strain behavior in the low BT content of the NBT–BT system.[14] Simons *et al.* found that the electric field transformed 0.96NBT–0.06BT predominantly to rhombohedral with a higher degree of structural distortion and proposed that the electric field-induced structural effects contribute significantly to the macroscopic strain and polarization of this system.[15] Thus, it is clearly evident that the electric field is found to alter the structural phase stabilization, MPB boundaries, and also could address the origin of the piezoelectric properties. Though there are several NBT-based binary solid solutions reported earlier, electric field driven studies and their structure property correlation are limited to a very few systems.[14–18] In this present study, we have developed a solid solution system based on $Ba_{0.85}Ca_{0.15}Ti_{0.9}Zr_{0.1}O_3$ (BCZT) and NBT. In our earlier studies, we had developed soft BCZT having a coercive field (E_C) of ~1–2 kV/cm, remanent polarization (P_r) of 11–12 μC/cm^2, and excellent piezoelectric response with a d_{33} of 500–600 pC/N.[19] Since BCZT stabilizes with tetragonal symmetry at room temperature, the formation of solid solution of NBT with BCZT could enhance the piezoelectric properties and reduce E_C.[20] Among the series of NBT–BCZT solid solutions developed, a composition near the vicinity of MPB, namely, 0.94NBT–0.06BCZT, is found to show enhanced ferro and piezoelectric properties (see the supplementary material).[21] The electric field driven study in the NBT–BCZT system is first of its kind in this system and has not been studied in the past. Hence, in this study, we intend to understand the structure property correlation through electric field-driven studies in the 0.94NBT–0.06BCZT system.

II. EXPERIMENTAL SECTION

Polycrystalline dense NBT and 0.94NBT–0.06BCZT ceramics were prepared by the conventional solid-state reaction technique. High purity (99.99% from Sigma Aldrich, USA) Na_2CO_3, Bi_2O_3, $BaCO_3$, $CaCO_3$, TiO_2, and ZrO_2 powders were used as precursors. Detailed preparation and processing conditions for NBT were discussed in our previous reports.[8,9] Prior to solid solution formation, $Ba_{0.85}Ca_{0.15}Ti_{0.90}Zr_{0.10}O_3$ (BCZT) powders were prepared by mixing desired stoichiometric amounts of precursors followed by calcination at 800 °C/3 h. The calcined NBT and BCZT-0.06 powders were mixed together to get 0.94NBT–0.06BCZT solid solution (*this composition will be hereafter referred to as BCZT-0.06*). These mixed powders were calcined again at 800 °C/3 h. The calcined BCZT-0.06 powders were ball-milled for 5 h using the 2-propanol medium and the milled slurries were dried at 80 °C. The dried powders were granulized using 1 wt. % polyvinyl alcohol (PVA) binder and compacted by uniaxial pressing. The green pellets of both BCZT-0.06 and NBT were sintered at 1150 °C/3 h in a covered alumina crucible. X-ray diffraction patterns were collected using PANalytical X'pert pro equipped with a Cu-Kα ($\lambda = 1.5406$ Å) radiation source. Neutron diffraction was carried out using neutrons of wavelength 1.48 Å on an four circle diffractometer (FCD) (PD-3) diffractometer at Dhruva Reactor, Trombay, India. Laser micro-Raman spectrometer (Senterra, Bruker) with an excitation source of 532 nm and 10 mW power was used to record the Raman active phonon modes. Microstructure and elemental mapping were carried out using a Field Emission Scanning Electron Microscope (FE-SEM) (Supra-40, Carl Zeiss, UK). Polarization vs electric field and unipolar strain vs electric field measurements were measured at 1 Hz using a triangular wave form in a TF-Analyzer 2000 (aixACCT systems, GmbH). Electrical poling was carried out using a DC power supply on gold sputtered specimens. Diffuse reflectance UV–Vis spectra were measured using a Shimadzu UV–VIS–near-infrared spectrophotometer having a resolution of ±1 nm.

III. RESULTS AND DISCUSSION

Figure 1(a) shows the polarization (P) vs electric field (E) hysteresis loops for NBT and BCZT-0.06 specimens. The P–E curves for BCZT-0.06 depict a well-squared hysteresis loop similar to that of NBT. It is evident from the P–E curves that BCZT-0.06 shows a polarization maximum (P_{max}) of ~41.5 μC/cm^2 which is slightly

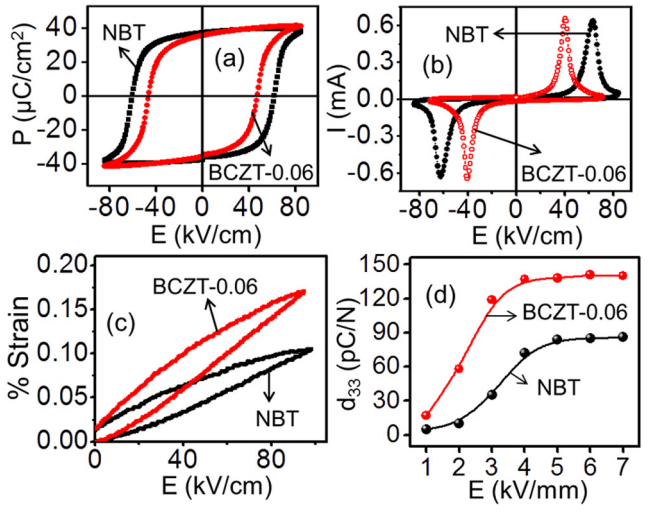

FIG. 1. (a) Polarization (P) vs electric field (E) hysteresis loops and their corresponding (b) switching current (I) curves for NBT and BCZT-0.06 specimens. (c) Unipolar strain (%S) vs electric field (E) curves and (d) electric field poling dependence of longitudinal piezoelectric charge coefficient (d_{33}) values for NBT and BCZT-0.06 specimens.

Published under license by AIP Publishing.

higher than NBT ($P_{max} \sim 39\,\mu C/cm^2$), whereas the remanent polarization (P_r) value for BCZT-0.06 is ~35.5 $\mu C/cm^2$ which is slightly less than NBT ($P_r \sim 37\,\mu C/cm^2$). Interestingly, the coercive field (E_C) for BCZT-0.06 has reduced significantly to ~39.5 kV/cm which is ~38% less as compared to NBT ($E_C = 63$ kV/cm). The sharp switching current (I) curves [see Fig. 1(b)] observed in both the specimens portray their intrinsic strong ferroelectric character.[8,22] The unipolar strain vs electric field curves as shown in Fig. 1(c) portray that NBT has a maximum strain of ~0.10%, whereas BCZT-0.06 displays an enhanced strain of ~0.17%, which is ~70% higher as compared to NBT. A lower degree of strain hysteresis is one of the important parameters for actuator applications, which is determined using the following equation: $\eta = \left[\Delta S_{\frac{E_{max}}{2}}/S_{max}\right] \times 100\%$, where $\Delta S_{\frac{E_{max}}{2}}$ is the deviation in unipolar strain during forward and reverse biasing measured at half of the applied electric field, i.e., $E_{max}/2$.[23] The degree of strain hysteresis (η) calculated using the aforementioned equation for BCZT-0.06 (~21.3%) is found to be less than that of NBT (~25.5%). Figure 1(d) shows the evolution of longitudinal small signal piezoelectric charge coefficient (d_{33}) values for both NBT and BCZT-0.06 with respect to the poling field. In the case of NBT, it is clearly evident that upon increasing the poling field, the d_{33} value increases slowly and above a threshold field, i.e., >5 kV/mm, the d_{33} value almost saturates around ~85 pC/N until 7 kV/mm. In the case of the BCZT-0.06 specimen, there is a slight increase in the d_{33} value even at lower poling fields, i.e., below 2 kV/mm. Whereas above 2 kV/mm, the d_{33} value increased rapidly and attained a maximum of ~145 pC/N at 4 kV/mm and remained invariable until 7 kV/mm for BCZT-0.06. Thus, an increase in the d_{33} value of ~70%, ~64% increase in %Strain values, ~38% softening in E_C, and ~17% decrease in degree of hysteresis (η) as compared to NBT are a remarkable feature in BCZT-0.06 and found to be a promising candidate for non-resonance mode actuator applications. The observed enhanced piezoelectric properties in BCZT-0.06 are comparable to several other reported lead free near MPB binary solid solutions, such as NBT–BT, NBT–KBT, etc.[24,25]

FE-SEM microstructure of the sintered NBT and BCZT-0.06 specimens is shown in Figs. 2(a) and 2(b). It is evident from the microstructure that both NBT and BCZT-0.06 have equiaxed densely packed grains. Interestingly, BCZT-0.06 displays an average grain size of ~3 μm, which is almost four times smaller (i.e., ~78% decrease in size) than NBT (~14 μm) as evidenced from the grain size distribution histograms shown in Figs. 2(c) and 2(d). The decrease in grain size in the BCZT-0.06 specimen could be attributed to the effect of larger cations, namely, Ba and Zr ions in the host lattice. These aforementioned larger cations act as pinning sites, thereby reducing the lattice diffusivity during the sintering process which in turn could lead to grain size refinement.[22] Figure 2(e) shows the higher magnification micrograph of BCZT-0.06, which clearly depicts well resolved grains without any phase segregation across the grain boundaries which in turn supports complete solubility of BCZT upon sintering. In addition, the elemental mapping of selected elements Ba, Zr, and Ca [see Figs. 2(f)–2(h)] over a selected region reflects the microstructural chemical homogeneity in the BCZT-0.06 specimen.

X-ray diffraction (XRD) patterns of the sintered NBT and BCZT-0.06 specimens shown in Fig. 3(a) exhibit perovskite phase formation, without observation of any secondary or impurity phases. As compared to NBT, all the Bragg peaks of BCZT-0.06 have a lower degree shift in their 2θ positions, as shown in the insets of Fig. 3(a). The lower degree 2θ shift observed in BCZT-0.06 could be attributed to the increment in d-spacing due to solid solution formation, i.e., larger ionic radii cations occupying both A-site as well as B-site, i.e., $Ba^{2+} = 1.61$ Å substituted at A-site ($Na^{1+} = 1.39$ Å/$Bi^{3+} = 1.36$ Å) and $Zr^{4+} = 0.72$ Å substituted at B-site ($Ti^{4+} = 0.605$ Å), respectively. It is known that the observation of superlattice (SL) Bragg reflections [i.e., ½(311)] arising due to the anti-phase tilting ($a^-a^-a^-$) of oxygen octahedra is a characteristic feature for $R3c$ symmetry.[8,9] However, the inset shown in Fig. 3(a) as indicated by arrow clearly depicts that there is a suppression in the intensity of ½(311) reflection for BCZT-0.06 as compared to NBT. The aforementioned variation in ½(311)

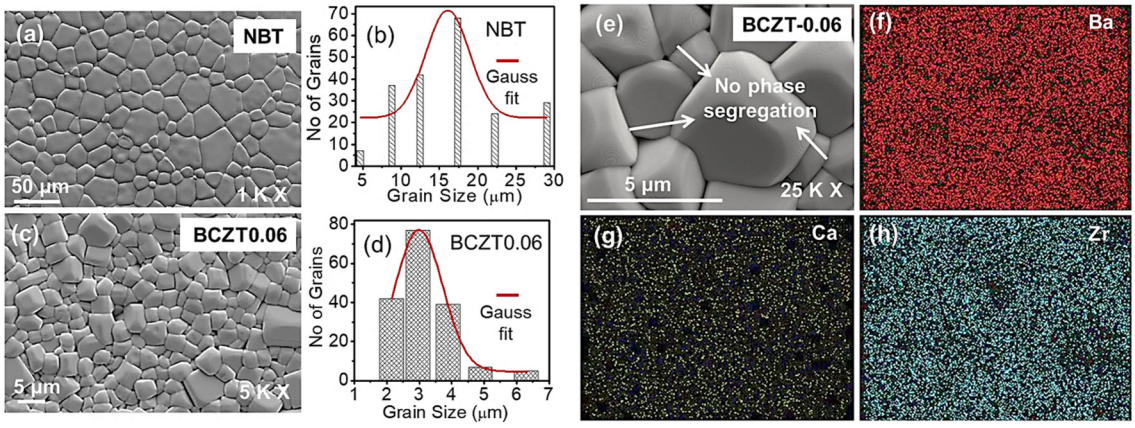

FIG. 2. (a)–(d) FE-SEM micrograph of sintered NBT and BCZT-0.06 specimens along with their corresponding grain size distribution. (e) Higher magnification micrograph of BCZT-0.06 and the elemental mapping corresponding to (f) Ba, (g) Ca, and (h) Zr.

Published under license by AIP Publishing.

reflection indicates the possibility of change in the tilt system for the BCZT-0.06 specimen due to structural distortion.[22] The structural distortion observed in BCZT-0.06 can be quantified based on the tolerance factor (τ) as per the equation as follows:

$$\tau = \frac{\langle (0.94 \times (0.5R_{Na} + 0.5R_{Bi})) + (0.06 \times (0.85R_{Ba} + 0.15R_{Ca})) \rangle + R_O}{\sqrt{2} \times (\langle (0.94 \times R_{Ti}) + (0.06 \times R_{Zr}) \rangle + R_O)},$$

where R_{Na}, R_{Bi}, R_{Ba}, and R_{Ca} are the 12-coordinated (CN) ionic radii corresponding to Na^{1+}, Bi^{3+}, Ba^{2+}, and Ca^{2+}, respectively; R_{Ti} and R_{Zr} are the 6-CN ionic radii corresponding to Ti^{4+} and Zr^{4+}, respectively; and R_O is the ionic radii of oxygen with 12-CN. Based on the above equation, the τ-factor for BCZT is found be 0.983, whereas for NBT, the calculated τ-factor is 0.978. It is known that perovskites with τ-factor between $0.985 < \tau < 1.06$ are expected to have un-tilted structures; anti-phase tilting for $0.964 < \tau < 0.985$; both anti-phase and in-phase tilting for $\tau < 0.964$.[26,27] The calculated τ-factor for BCZT-0.06 lies on the boundary between anti-phase and un-tilted structure systems. Hence, from the aforementioned variations observed in the XRD pattern and the τ factor, it is evident that there is a possibility of structural distortion on a global scale in the BCZT-0.06 specimen due to solid solution formation.

Figure 3(b) shows the Raman scattering spectra of the sintered NBT and BCZT-0.06 specimens. The observed Raman scattering spectra show four major broad intense bands which are designated as bands A–D as shown in Fig. 3(b). Based on the first-principles density functional theoretical analysis of our previous study, the phonon modes for parent NBT are assigned as follows: the low frequency mode from 109 to 134 cm^{-1} (Bi–O) and 155 to 187 cm^{-1} (Na–O) has been assigned collectively to A_{site}-O (A_{site} = Bi/Na) vibrations (band A); strong high intense band from 246 to 401 cm^{-1} belongs to Ti–O vibrations (band B); mid-frequency vibrations from 413 cm^{-1} are associated with TiO_6 vibrations (band C); and high frequency modes above ~700 cm^{-1} are assigned to oxygen displacements (band D).[9,28] As compared to NBT, Raman spectra of BCZT-0.06 depict noticeable variations in bands A, B, and C, respectively. The band A (i.e., $\omega_{A\text{-}O}$) centered around 140 cm^{-1} displays two significant variations in BCZT-0.06 as compared to NBT, i.e., a large softening in phonon frequency of ~23 cm^{-1} and a strong suppression in the intensity of the $\omega_{A\text{-}O}$ band as shown in the inset of Fig. 3(b). As per the relation between reduced mass (m^*) and frequency (ω) (i.e., $\omega = \sqrt{k/m^*}$, where k is the force constant), an obvious phonon softening in $\omega_{A\text{-}O}$ is expected when an ion with larger mass and larger size is substituted at A-site (m_{Na} = 22.989 g/mol, m_{Bi} = 208.980 g/mol, m_{Ba} = 137.327 g/mol, and m_{Ca} = 40.078 g/mol).[24] Hence, the softening and intensity variation collectively observed in the $\omega_{A\text{-}O}$ band of BCZT-0.06 is attributed to the substitution of Ba and Ca ions at A-site. The band B (i.e., ω_{Ti-O}) centered around 275 cm^{-1} is found to show an increase in phonon line width, i.e., Full Width at Half Maximum (FWHM) (Γ) of ~31 cm^{-1} and appearance of a pronounced shoulder in the ω_{Ti-O} phonon profile around 300 cm^{-1} for BCZT-0.06 as compared to NBT. The increase in Γ and variation in the ω_{Ti-O} band profile indicate a local structural disorder at

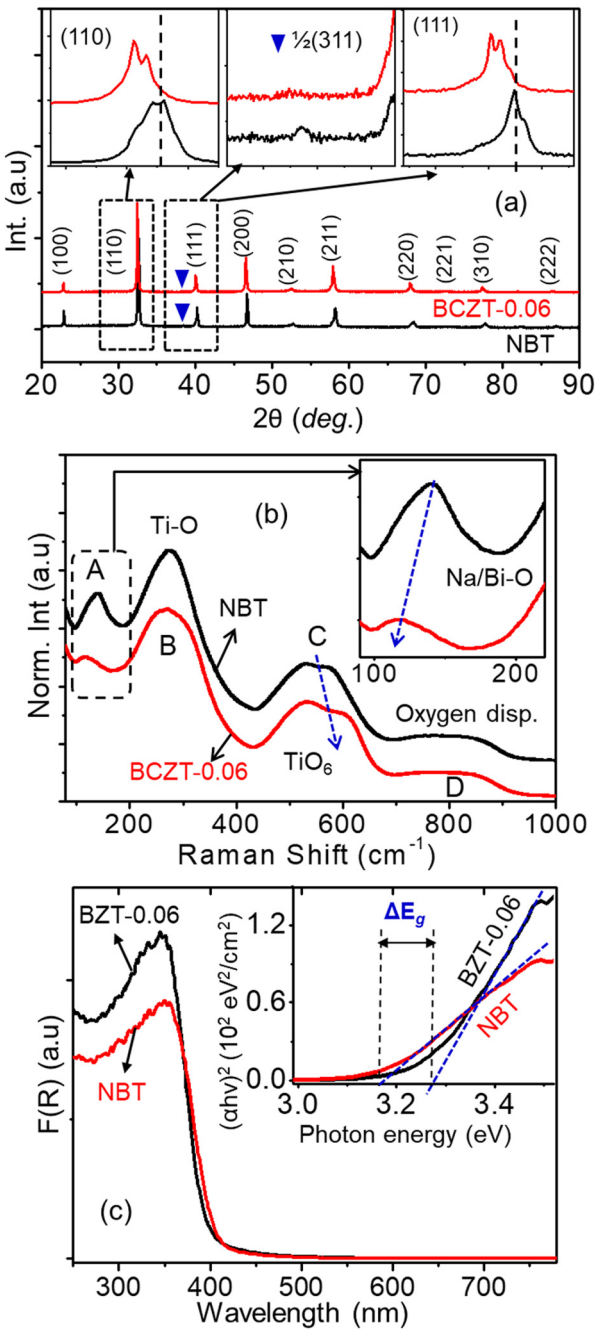

FIG. 3. (a) X-ray diffraction pattern, (b) Raman scattering spectra, and (c) UV–Vis spectra for sintered NBT and BCZT-0.06 specimens.

Ti–O bond due to a cation of larger mass (m) (m_{Ti} = 47.86 g/mol, m_{Zr} = 91.22 g/mol) and radii substituted at B-site.[9]

Thus, the observed variations in the ω_{Ti-O} band of BCZT-0.06 indicate that Zr-ion gets substituted at Ti-site of the host lattice.

Published under license by AIP Publishing.

The band C (i.e., ω_{TiO_6}) centered at ~550 cm^{-1} displays a noticeable hardening in the phonon frequency of ~20 cm^{-1} [see Fig. 3(b), indicated by arrow] and an increase in Γ of ~14 cm^{-1} for BCZT-0.06 when compared with NBT. As per hard mode spectroscopy concepts, hardening and variation in the band profile of octahedral phonon modes is an indicator for the octahedral tilt transition from the parent tilt system.[9,29] All these aforementioned variations in ω_{A-O}, ω_{Ti-O}, and ω_{TiO_6} for BCZT-0.06 strongly portray the local structure distortion as a consequence of solid solution formation.

Figure 3(c) shows the absorbance spectra of NBT and BCZT-0.06 specimens. The optical absorbance $F(R)$ is derived from the reflectance using the Kubelka Munk equation

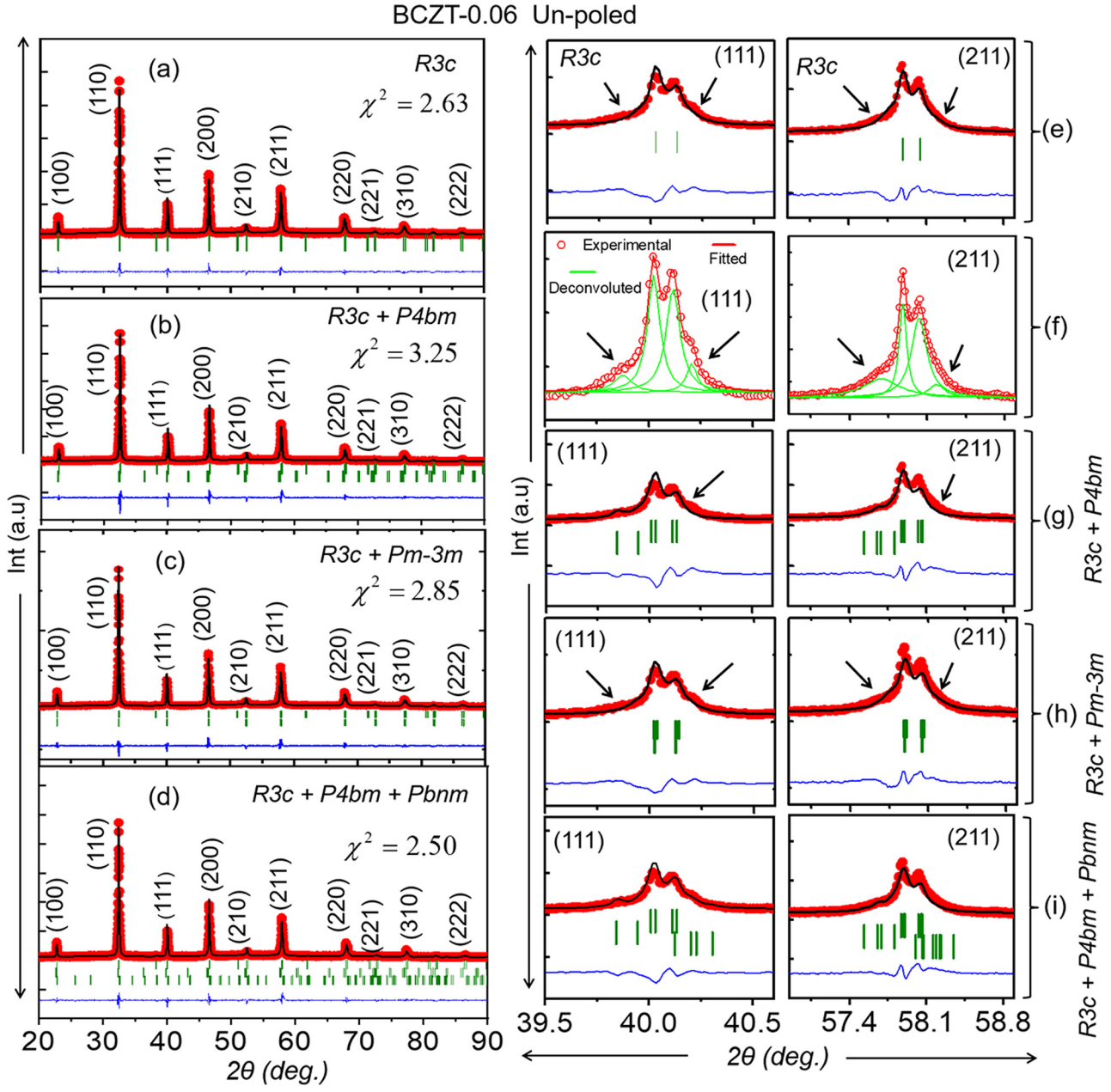

FIG. 4. Rietveld refined XRD pattern of the unpoled BCZT-0.06 specimen fitted using different structural models, viz., (a) *R3c*, (b) *R3c* + *P4bm*, (c) *R3c* + *Pm-3m*, and (d) *R3c* + *P4bm* + *Pbnm*. Close observation of (111) and (211) Bragg reflection corresponding to (e) *R3c*, (g) *R3c* + *P4bm*, (h) *R3c* + *Pm-3m*, and (i) *R3c* + *P4bm* + *Pbnm*.

Published under license by AIP Publishing.

TABLE I. Rietveld refined structural and fitting parameters corresponding to the x-ray diffraction pattern of the BCZT-0.06 specimen fitted using the *R3c* + *P4bm* + *Pbnm* structural model.

R3c	*x*	*y*	*z*
Na/Bi/Ca/Ba	0	0	0.2569 (1)
Ti/Zr	0	0	0.0073 (3)
O	0.1483(2)	0.3460 (1)	0.0833[a]
$a = 5.5128$ (5) Å, $c = 13.5077$ (2) Å, $V = 355.521$ (1) Å^3, Bragg R-factor= 4.26, R_F-factor = 3.01			
P4bm	*x*	*y*	*z*
Na/Bi/Ca/Ba	0	0.5	0.4451 (9)
Ti/Zr	0	0	0
O1	0	0	0.7589 (9)
O2	0.2796 (3)	0.2203 (7)	0.0150 (1)
$a = 5.5300$ (5) Å, $c = 3.9255$ (5) Å, $V = 120.049$ Å^3, Bragg R-factor = 5.88, R_F-factor = 4.99			
Pbnm	*x*	*y*	*z*
Na/Bi/Ca/Ba	0.0010 (1)	0.4936 (6)	0.2500
Ti/Zr	0	0	0
O1	−0.0570 (1)	0.0020 (1)	0.2500
O2	0.2519 (2)	0.2576 (1)	0.0260 (1)
$a = 5.4940$ (5) Å, $b = 5.4826$ (2) Å, $c = 7.7889$ (2) Å, $V = 234.616$ Å^3, Bragg R-factor = 6.47, R_F-factor = 6.99			
R_p, 5.25; R_{wp}, 6.89; R_{exp}, 4.37; χ^2, 2.49			
Phase fraction			
R3c = 80.07(0.60)%, *P4bm* = 10.37(0.08)%, *Pbnm* = 9.56(0.23)%			

[a]O(z) fixed as floating origin.

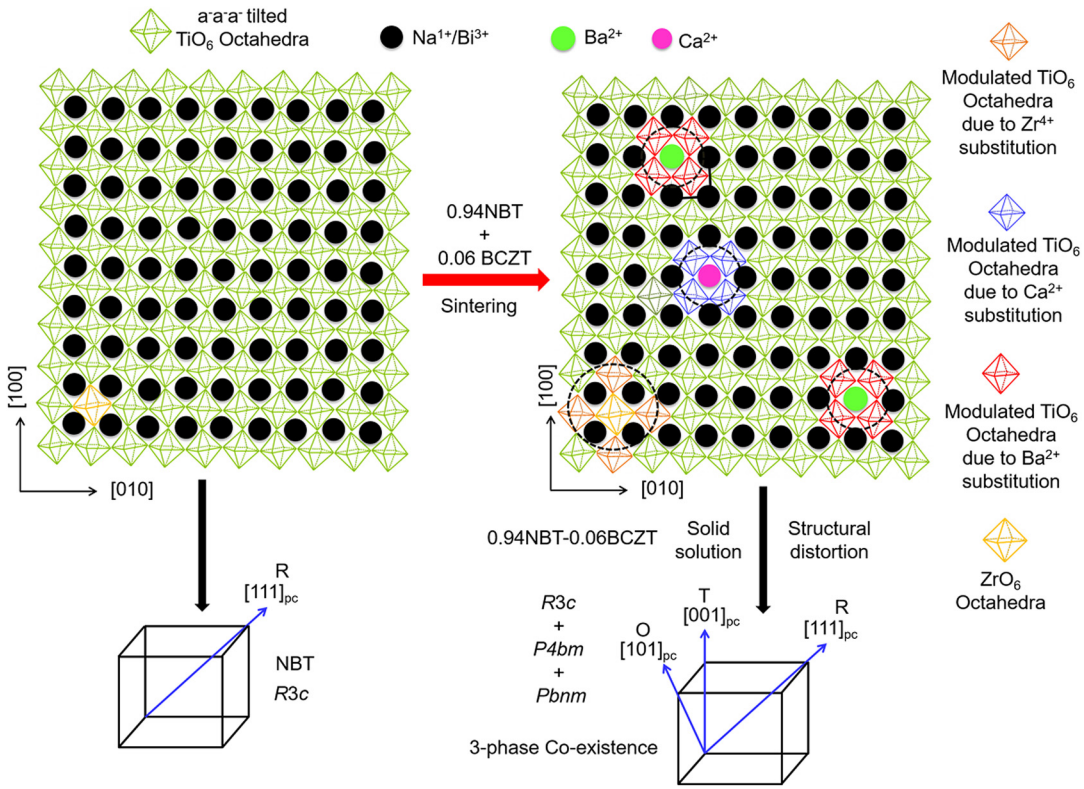

FIG. 5. Schematic representation indicating structural distortion in the BCZT-0.06 specimen due to solid solution formation.

Published under license by AIP Publishing.

$F(R) = (1-R)^2/2R = \alpha/s$ (where R is the reflectance, α is absorption coefficient, and s is the scattering coefficient).[27] The optical absorbance curves are converted to Tauc plot of $(\alpha h\nu)^n$ against the photon energy using the Tauc equation $(\alpha h\nu)^n = A(h\nu - E_g)$, where A is a constant, E_g is the optical bandgap energy, $h\nu$ is the energy of incident photon, and n is an index determined by the nature of the electron transition during the absorption process ($n = 1/2$, 2, 3/2, or 3 *for direct allowed, indirect allowed, direct forbidden, and indirect forbidden transitions*, respectively).[30] The electronic transition in NBT-based systems has been reported as indirect allowed transition; hence, n as 2 is used in this present study.[30] It is evident from the close observation of the Tauc plot [see the inset of Fig. 3(c)] that the absorption edge of BCZT-0.06 shows a noticeable variation as compared to NBT. The bandgap energies (E_g) for NBT and BCZT-0.06 are determined by extrapolating the linear part of the $(\alpha h\nu)^2$ plot to 0 and are found to be 3.16 and 3.26 eV, respectively. The E_g value of NBT determined in this study is similar to that of the value observed in earlier reports.[30,31] Eng *et al.* reported that in perovskite oxides, the occurrence of an octahedral tilt distortion can increase the bandgap by ~0.5 eV due to the distortion in the linear B–O–B bonds, thereby narrowing the conduction band.[32] It has been reported that in ferroelectric perovskites, the bandgap has a strong sensitivity to the octahedral tilting, lattice strain, and local cation displacements.[33,34] Hence, the increase in band transition energy observed in BCZT-0.06 could be attributed to the octahedral tilt transition, as discussed in the aforementioned section. In addition to the octahedral tilt transition, lattice distortion at both A-site and B-site due to Ba^{2+}, Ca^{2+}, and Zr^{4+} ions and interaction of these ions with the TiO_6 octahedral network will lead to a complex energy distribution, therefore may lead to a change in the band transition energy in BCZT-0.06.[32] It is clearly evident from UV–Vis spectroscopic results that there is a subtle change observed even in the electronic structure of BCZT-0.06 as compared to NBT.

Rietveld analysis for both BCZT-0.06 and NBT is carried out in order to address the global structural distortion in detail. In our previous studies, XRD pattern of NBT was fitted using an *R3c* structural model.[8,9,28] Hence, in this present study, *R3c* space group is used for fitting the XRD pattern of NBT (see the supplementary material). Similarly for BCZT-0.06, the *R3c* structural model is adapted and the entire XRD pattern is found to fit well with the *R3c* space group as shown in Fig. 4(a). However, upon close observation of selected Bragg peaks, viz., $(111)_{pc}$ and $(211)_{pc}$, there are some unindexed Bragg reflections observed both on the lower as well as higher angle side as shown in Fig. 4(e) marked by arrows. In order to clearly visualize the unindexed reflections, $(111)_{pc}$ and $(211)_{pc}$ Bragg peaks are de-convoluted into their individual components as shown in Fig. 4(f). The de-convoluted Bragg peaks reveal the unindexed reflections and indicate the possibility of multiple phase co-existence along with the *R3c* structure in the BCZT-0.06 specimen.

It is known that in $(1-x)$ NBT–$(x)BaTiO_3$-based solid solution, the structure of a near MPB composition (i.e., $x = 0.06$) has been reported to stabilize in different forms, viz., *R3c* + *Pm-3m*, *Cc* + *Pm-3m*, *R3c* + *P4bm*, etc. Recently, Rao *et al.* observed a three-phase co-existence of *Pm-3m* + *R3c* + *P4mm* in a near MPB composition ($x = 0.06$) of the NBT–BT system.[35] Since BCZT-0.06 is slightly similar to NBT–BT, several structural models are to be

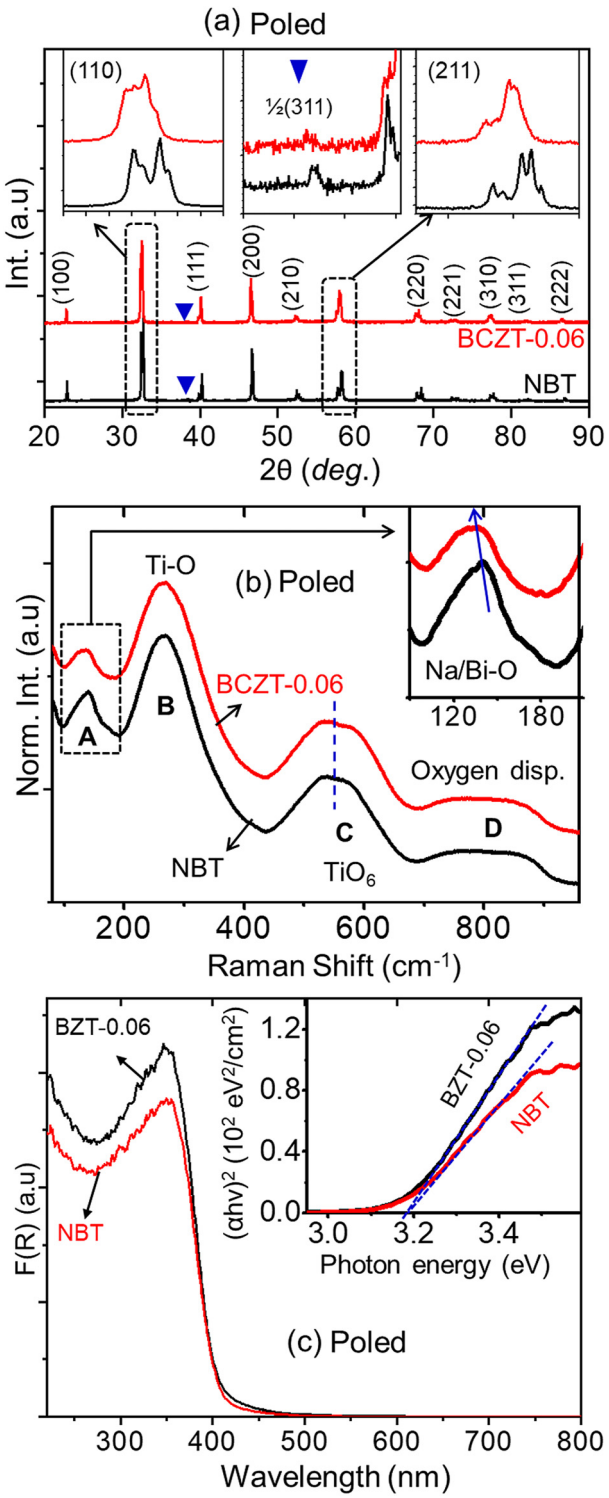

FIG. 6. (a) X-ray diffraction patterns, (b) Raman scattering spectra, and (c) UV–Vis spectra for poled NBT and BCZT-0.06 specimens.

Published under license by AIP Publishing.

explored to fit the unindexed Bragg reflections observed in $(111)_{pc}$ and $(211)_{pc}$ Bragg peaks. It is known that parent BCZT stabilizes in *P4mm* symmetry at room temperature. Hence, the *R3c* + *P4mm* model is executed initially for fitting the XRD pattern of BCZT-006. However, this model has failed to fit the entire pattern. *P4bm* is known to be the high temperature phase of parent NBT; hence, a combination of the *R3c* + *P4bm* structural model has been considered and could fit the entire pattern [see Fig. 4(b)]. It is evident that the *R3c* + *P4bm* model could suitably index the lower degree Bragg reflections as shown in Fig. 4(g). However, the higher angle reflection could not be indexed using the *R3c* + *P4bm* structural model [see Fig. 4(g), marked by arrow]. Furthermore, the analysis is extended by considering the *R3c* + *Pm-3m* space group [see Fig. 4(c)]. However, both the lower and higher degree Bragg reflections are not indexed by using the *R3c* + *Pm-3m* model as shown in Fig. 4(h). In this regard, Rietveld analysis has been carried out by considering a three-phase structural model, viz., *R3c* + *P4bm* + *Pbnm* corresponding to rhombohedral (R), tetragonal (T), and orthorhombic (O) phases, respectively. After adopting the three-phase model, all the unindexed Bragg reflections observed in $(111)_{pc}$ and $(211)_{pc}$ Bragg peaks of BCZT-0.06 are indexed and fitted well as shown in Fig. 4(i). The Rietveld refined plot of the BCZT-0.06 specimen fitted using the *R3c* + *P4bm* + *Pbnm* model fits the entire pattern well with a better goodness of fitting parameter (i.e., $\chi^2 = 2.50$) as compared to the *R3c* model ($\chi^2 = 2.63$) as shown in Fig. 4(d). The phase fraction of each phase in BCZT-0.06 and their structural and fitting parameters are shown in Table I. In the BCZT-0.06 specimen, both A-site and B-site are highly disordered due to Ba^{2+}, Ca^{2+}, and Zr^{4+} cations occupying their respective sites of the host NBT lattice due to solid solution formation. The complex cationic nature in BCZT-0.06 induces significant modulation in the local octahedral network thereby inducing tilt disorder (see Fig. 5) and resulted in a three-phase co-existence of R + T + O, respectively.

In our recent study, electric field-induced structural distortion is observed in parent NBT. Upon poling both A-site and B-site, cations displayed pronounced displacement along the polar [111] direction leading to the polarization extension mechanism.[8] The proposed mechanism could explain electric field dependence of piezoelectric properties in NBT. Hence, for understanding the origin of enhanced piezoelectric properties observed in the BCZT-0.06 specimen, a detailed analysis of the poled structure at different length scales, namely, global, local, and electronic, could give us the one-to-one correspondence in terms of the structure property correlation. Figure 6(a) shows the x-ray diffraction patterns of NBT and BCZT-0.06 recorded after poling the specimens. It is clearly evident that in both poled NBT and BCZT-0.06, there is a noticeable variation in the Bragg profile as compared to that of the unpoled specimens. Interestingly, the intensity of ½(311) reflection gets pronounced in BCZT-0.06 upon poling when compared with the unpoled state. Figure 6(b) shows the Raman scattering spectra of poled NBT and BCZT-0.06. In the poled BCZT-0.06 specimen, the $\omega_{A\text{-}O}$ mode shows a softening of ~4 cm^{-1} as compared to poled NBT [see the inset of Fig. 6(b)]. It is to be noted that in the unpoled state, the softening observed between BCZT-0.06 and NBT in the $\omega_{A\text{-}O}$ mode is ~23 cm^{-1}. Similarly, in the case of the ω_{Ti-O} mode, FWHM (Γ) has reduced to ~15 cm^{-1} from ~31 cm^{-1}, whereas in the ω_{TiO_6} mode, the hardening in the

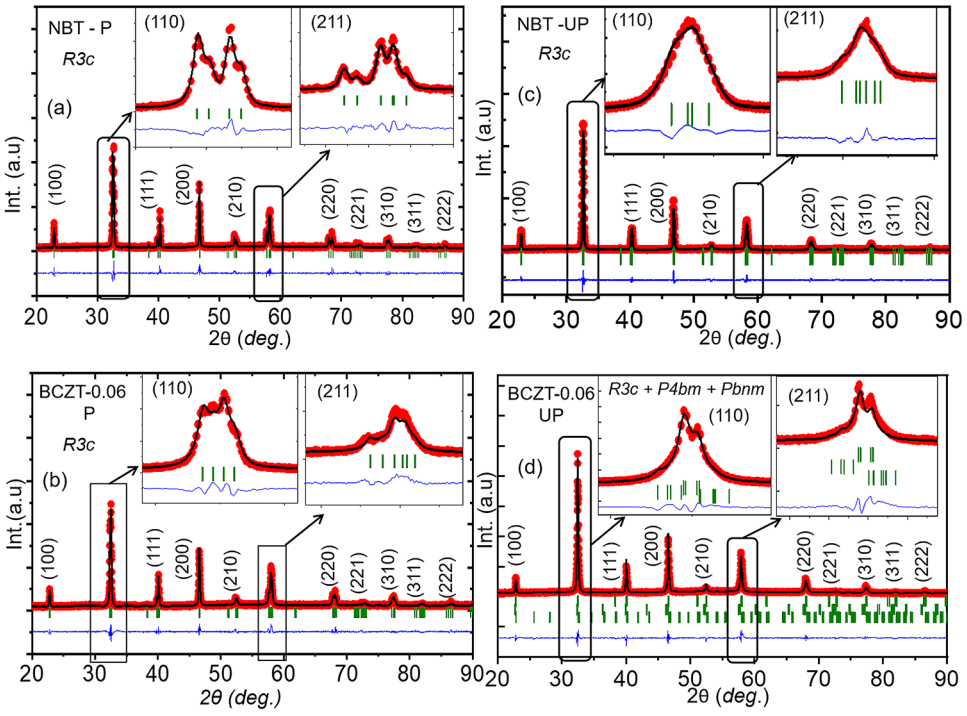

FIG. 7. Comparison of Rietveld refined x-ray diffraction patterns corresponding to (a) poled NBT, (b) poled BCZT-0.06, (c) unpoled NBT, and (d) unpoled BCZT-0.06 specimens.

Published under license by AIP Publishing.

phonon frequency has reduced to ~2 cm^{-1} from ~20 cm^{-1} in the poled BCZT-0.06 specimen. A reduced hardening in the ω_{TiO_6} mode of poled BCZT-0.06 indicates that electric field drives the local octahedral instabilities to an ordered state.[7,9] The ordering in the octahedral chains reduces the local structural disorder which also gets reflected in the $\omega_{A\text{-}O}$ and ω_{Ti-O} mode, viz., reduced softening in the phonon frequency of the $\omega_{A\text{-}O}$ mode and reduced FWHM (Γ) of the ω_{Ti-O} mode. It is clearly evident that upon poling, both BCZT-0.06 and NBT specimens show a similar Raman spectrum. Hence, on a local scale, the electric field drives the structure of BCZT-0.06 to *R*3*c* as that of NBT. Figure 6(c) shows the absorbance spectra of poled NBT and BCZT-0.06 specimens. It is evident that the absorption edge for BCZT-0.06 and NBT looks similar upon poling. The optical bandgap (E_g) obtained from the Tauc plot as shown in the inset of Fig. 6(c) is found to be ~3.17 eV for both poled BCZT-0.06 and NBT. Thus, it is clear that the electric field alters the electronic structure of BCZT-0.06 similar to NBT upon poling, hence *R*3*c* phase stabilization in BCZT-0.06 after poling.

Rietveld analysis of the XRD pattern corresponding to poled NBT and BCZT-0.06 is shown in Figs. 7(a) and 7(b). It is evident from the Rietveld analysis that the entire XRD pattern for both NBT and BCZT-0.06 fits well with the *R*3*c* structural model. The insets shown in Figs. 6(a) and 6(b) for selected (110) and (211) Bragg peaks strongly support the goodness of Rietveld fit using the *R*3*c* model [in view of better readability, a comparison between the Rietveld fits of unpoled NBT and unpoled BCZT-0.06 is shown in Figs. 7(c) and 7(d) along with the poled specimens]. In order to further understand the detailed structural aspects, especially the octahedral dynamics, neutron diffraction (ND) measurements are performed on poled NBT and poled BCZT-0.06 specimens.

In a similar manner as that of XRD, the ND pattern corresponding to both poled NBT and BCZT-0.06 has been fitted using the *R*3*c* structural model. Interestingly, both NBT and BCZT-0.06 fitted extremely well with the *R*3*c* space group [see Figs. 8(a) and 8(b)] and the insets shown strongly portray the goodness-of-fit obtained using the *R*3*c* structural model. The ½(311) superlattice reflections corresponding to the anti-phase tilting of oxygen octahedra were found to be intense and more pronounced in the ND pattern of the poled specimens. These intense ½(311) reflections strongly portray the *R*3*c* phase stabilization in both poled NBT and BCZT-0.06. The structural parameters deduced from the Rietveld fits of the ND pattern are shown in Table II. It is clearly evident that there is an increase in the unit cell volume and a decrease in the *c*/*a* ratio for poled BCZT-0.06 as compared to that of poled NBT (see Table II). It is known that small rhombohedral lattice distortion and minimum homogeneous strain are one of the primary intrinsic parameters which favors the non-180° domain re-orientation, domain switching, and domain wall motion and results in enhanced piezoelectric properties.[4] In this regard, rhombohedral lattice distortion (δ_r) is calculated from the *d*-spacing of (111) and (−111) Bragg reflections using the equation $\delta_r = (9/8)[(d_{111}/d_{11-1}) - 1]$ (Table II).[4]

The δ_r values obtained for poled NBT and poled BCZT-0.06 are found to be 0.0093 and 0.0078, respectively. It is evident that there is a ~16% decrease in rhombohedral lattice distortion for poled BCZT-0.06 as compared to poled NBT. Homogeneous strain

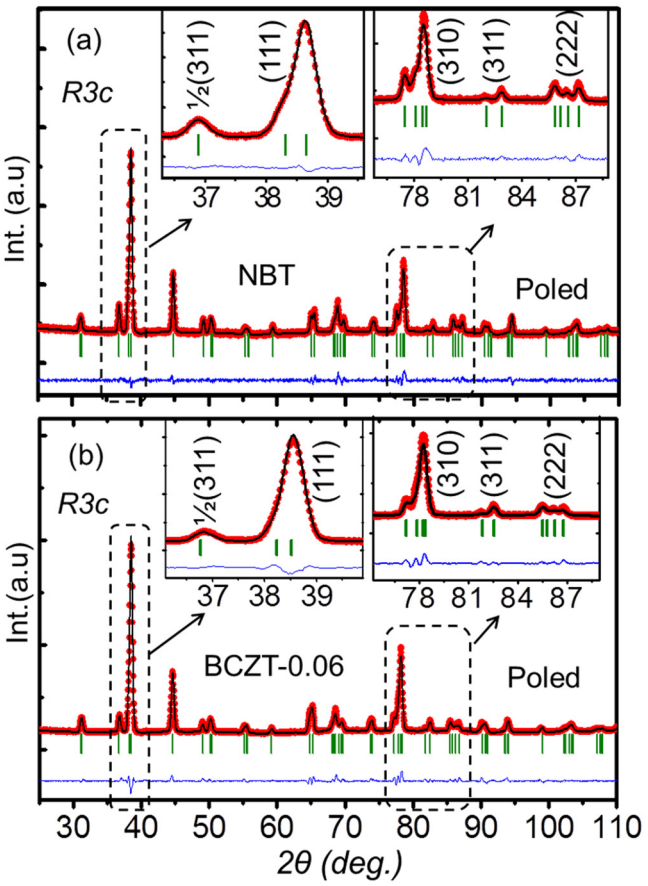

FIG. 8. Comparison of Rietveld refined neutron diffraction (ND) patterns of poled (P) specimens corresponding to (a) NBT and (b) BCZT-0.06 fitted using the *R*3*c* structural model. Insets in both (a) and (b) show the close observation of selected Rietveld refined Bragg reflections indicating the goodness-of-fit.

(δ) for the rhombohedral lattice with diagonal of the unit cell as polar axis can be calculated using $\delta = \pi/2 - \alpha$, where α is the deviation of the angle from 90° which is obtained from the hexagonal cell values as $\mathrm{Cos}\,\alpha = ((c^2/a^2) - 3/2)/((c^2/a^2) + 3)$.[4] The δ values for poled NBT and poled BCZT-0.06 are found to be 0.431 and 0.338, respectively. It is found that there is a ~21% decrease in homogeneous strain for poled BCZT-0.06 as compared to poled NBT. Smaller rhombohedral distortion lowers the deviation angle which in turn brings about a small strain in the poled BCZT-0.06 specimen.

Apart from the lattice distortion, cation displacements, octahedral distortion, and their dynamics also play a major role in determining the physical properties of perovskite structures. Hence, in order to understand structural distortion in detail, the atomic positional coordinates in terms of their fractional displacements as shown in Table III and octahderal dynamics are analyzed (see the supplementary material). The octahedral tilt angle (ω°) calculated using the expression $\omega = \tan^{-1}(4e3^{1/2})$ is found to be ~7.56° for

Published under license by AIP Publishing.

TABLE II. Crystallographic structural and fitting parameters for poled NBT and BCZT-0.06 specimens obtained from the Rietveld analysis of the neutron diffraction pattern.

Structural parameters	NBT-poled	BCZT-0.06 poled
Space group	*R3c*	*R3c*
a_H (Å)	5.4731(3)	5.4907 (7)
c_H (Å)	13.5385 (1)	13.5548 (1)
V (Å^3)	351.216 (7)	353.908 (1)
c/a ratio	2.4736	2.4686
s	0.0261	0.0249
t	0.0116	0.0128
d	−0.0014	−0.0013
e	0.0242	0.0191
$\omega°$	9.52	7.56
$\zeta \times 10^2$	−0.413	−0.097
δ_r	0.0093	0.0078
$\delta°$	0.431	0.338
R_p	2.15	2.60
R_{wp}	3.46	3.69
R_{exp}	1.66	1.25
χ^2	4.37	6.75

BCZT-0.06, which is ∼20% lower in magnitude than NBT, i.e., ∼9.52°. In perovskites, there is a homogeneous flattening or elongation of the octahedron along the triad axis described by a factor $1+\zeta$ which is referred to as octahedral strain.[36,37] The octahedral strain (ζ) is determined using the following expression: $\zeta = \cos\omega\omega\left(\frac{c_h}{6^{1/2}a_h}\right) - 1$.[36,37] It is evidenced that there is a significant decrease in octahedral strain of about ∼76% for poled BCZT-0.06 ($\zeta \times 10^2 = -0.097$) as compared to the poled NBT ($\zeta \times 10^2 = -0.413$) specimen. In addition to the rhombohedral lattice distortion and homogenous strain, cation displacements also influence the piezoelectric properties. The shifts of A-site (dodecahedron-AO_{12}) and B-site (octahedron-BO_6) cations along the ferroelectric axis (i.e., along [111]) of the *R3c* space group are derived from the Rietveld refined atomic positional parameters and referred to as *s* and *t*, respectively (see the supplementary material).[36,37] It is evidenced that there is a 10% increase in *t* parameter for poled BCZT-0.06 as compared to poled NBT (Table III). Thus, a notable increment in *t* parameter indicates pronounced B-site cation (Ti/Zr) displacement along the polar [111] axis.

TABLE III. Atomic fractional coordinates and their positions for poled NBT and BCZT-0.06 specimens.

Atomic species	*x*	*y*	*z*
Na/Bi	0	0	0.2761 (6)
Na/Bi/Ba/Ca	0	0	0.2749 (7)
Ti	0	0	0.0116 (8)
Ti/Zr	0	0	0.0127 (6)
O(z)	0.1212 (1)	0.3391 (2)	0.0833[a]
	0.1311 (4)	0.33876	0.0833[a]

[a]O(z) fixed as floating origin.

The pronounced B-site cation displacement indicates the increase in the strength of polarization and polarization extension mechanism in poled BCZT-0.06.[8] Thus, based on the ND analysis, it is clear that in poled BCZT-0.06 specimens, there is a smaller rhombohedral lattice distortion, reduced homogeneous strain, octahedral tilt angle, and octahedral strain. It is reported that in ferroelectric ceramics, approximately 35% of piezoelectric contribution is from non-180° domain switching.[38] Thus, the aforementioned intrinsic parameters, viz., smaller rhombohedral distortion, reduced homogeneous strain, and octahedral strain in BCZT-0.06, facilitate the non-180° domain re-orientation, domain switching, and domain wall motion which in turn leads to the enhanced piezoelectric properties and a decrease in the coercive field.

IV. CONCLUSION

In summary, it is clearly evidenced that due to solid solution formation in BCZT-0.06, there is a significant structural distortion leading to a three-phase mixture, viz., *R3c* + *P4bm* + *Pbnm* as compared to parent NBT (*R3c*). It is to be noted that the structural distortion gets reflected across different length scales, viz., global, local, and even in electronic structures, as evidenced from the x ray/Raman/UV–Vis results. Interestingly, upon electric field poling, the structural distortions observed at different length scales become ordered and lead to *R3c* phase stabilization in BCZT-0.06 with reduced lattice and octahedral strain as compared to parent NBT. As a result, there is an ease in non-180° domain switching in BCZT-0.06. In addition, the pronounced Ti-cation displacement along the polar [111] axis in BCZT-0.06 indicates the polarization extension mechanism. Thus, a combined effect of non-180° domain switching and polarization extension mechanism is found to be the origin of enhanced piezoelectric response in BCZT-0.06. The present study evidenced that the electric field-driven studies in the BCZT-0.06 specimen could address the origin of enhanced piezoelectric properties, and such studies can be extended to other potential piezoelectric systems to understand the structure property correlation and establish one-to-one correspondence with the observed piezoelectric properties.

SUPPLEMENTARY MATERIAL

See the supplementary material for the Rietveld fit of the entire XRD pattern of unpoled specimens under investigation, i.e., NBT and BCZT-0.06. Calculations for the octahedral strain and cation displacements from atomic positional coordinates are included in detail.

ACKNOWLEDGMENTS

S.A. and T.K. thank CSIR, India, for the financial support to carry out this work under the project CSIR-EMRII (Ref. No. 0194/NS) and the UGC-DAE Consortium for Scientific Research, Mumbai Center for availing the neutron diffraction facilities under Project Ref. No. CRS-M-250.

REFERENCES

[1]J. Koruza, A. J. Bell, T. Fromling, K. G. Webber, K. Wang, and J. Rodel, J. Materiomics **4**, 13 (2018).

Published under license by AIP Publishing.

[2]J. Rodel, K. G. Webber, R. Dittmer, W. Jo, M. Kiruma, and D. Damjanovic, J. Eur. Ceram. Soc. **35**, 1659 (2015).
[3]C.-H. Hong, H.-P. Kim, B.-Y. Cgoi, H.-S. Han, J. S. Son, C. W. Ahn, and W. Jo, J. Materiomics **2**, 1 (2016).
[4]W. Heywang, K. Lubitz, and W. Wersing, *Piezoelectricity-Evolution and Future of a Technology* (Springer Publications, 2008).
[5]B. Jaffe, W. R. Cook, Jr., and H. Jaffe, *Piezoelectric Ceramics* (Academic Press, New York, 1971).
[6]B. N. Rao and R. Ranjan, Phys. Rev. B **86**, 134103 (2012).
[7]B. N. Rao, R. Dutta, S. Selva Chandrasekaran, D. K. Mishra, V. Sathe, A. Senyshyn, and R. Ranjan, Phys. Rev. B **88**, 224103 (2013).
[8]T. Karthik and S. Asthana, J. Phys. D Appl. Phys. **50**, 385601 (2017).
[9]T. Karthik, D. Radhakrishanan, C. Narayana, and S. Asthana, J. Alloys Compd. **732**, 945–951 (2018).
[10]J. E. Daniels, W. Jo, J. Rodel, and J. L. Jones, Appl. Phys. Lett. **95**, 032904 (2009).
[11]G. Picht, J. Töpfer, and E. Hennig, J. Eur. Ceram. Soc. **30**, 3445 (2010).
[12]A. J. Royles, A. J. Bell, A. P. Jephcoat, A. K. Kleppe, S. J. Milne, and T. P. Comyn, Appl. Phys. Lett. **97**, 132909 (2010).
[13]M. Otoničar, S. D. Škapin, B. Jančar, and D. Suvorov, J. Appl. Phys. **113**, 024106 (2013).
[14]C. Ma, H. Guo, and X. Tan, Adv. Funct. Mater. **23**, 5261 (2013).
[15]H. Simons, J. Daniels, W. Jo, R. Dittmer, A. Studer, M. Avdeev, J. Rödel, and M. Hoffman, Appl. Phys. Lett. **98**, 082901 (2011).
[16]A. Mahajan, H. Zhang, J. Wu, E. Venkata Ramana, M. J. Reece, and H. Yan, J. Phys. Chem. C **121**(10), 5709–5718 (2017).
[17]G. Viola, H. Ning, M. J. Reece, R. Wilson, T. M. Correia, P. Weaver, M. G. Cain, and H. Yan, J. Phys. D Appl. Phys. **45**, 355302 (2012).
[18]X. Liu and X. Tan, Adv. Mater. **28**, 574–578 (2016).
[19]J. P. Praveen, T. Karthik, A. R. James, E. Chandrakala, S. Asthana, and D. Das, J. Eur. Ceram. Soc. **35**, 1785 (2015).
[20]L. Jin, W. Luo, L. Wang, Y. Tian, Q. Hu, L. Houa, L. Zhang, X. Lu, H. Du, X. Wei, G. Liu, and Y. Yan, J. Eur. Ceram. Soc. **39**, 277 (2019).
[21]T. Karthik, "Structure property correlation through electric field driven effects in lead free $Na_{0.5}Bi_{0.5}TiO_3$ based ferro/piezoelectric ceramics," Doctoral dissertation (Indian Institute of Technology Hyderabad, India, 2016).
[22]T. Karthik and S. Asthana, Mater. Lett. **190**, 273–275 (2017).
[23]H. Zhang, P. Xu, E. Patterson, J. Zang, S. Jiang, and J. Rödel, J. Eur. Ceram. Soc. **35**, 2501–2512 (2015).
[24]S. Priya and S. Nahm, *Lead Free Piezoelectrics* (Springer Publications, 2012).
[25]G. D. Adhikary, D. K. Khatua, A. Senyshyn, and R. Ranjan, Acta Mater. **164**, 749 (2019).
[26]P. Kumar, N. Shankhwar, A. Srinivasan, and M. Kar, J. Appl. Phys. **117**, 194103 (2015).
[27]K. Thangavelu, T. Durga Rao, A. Srinivas, and S. Asthana, J. Mater. Sci. Mater. Electron. **26**, 8676 (2015).
[28]M. K. Niranjan, T. Karthik, S. Asthana, J. Pan, and U. V. Waghmare, J. Appl. Phys. **113**, 194106 (2013).
[29]E. K. H. Salje and U. Bismayer, Phase Transit. **63**, 1–75 (1997).
[30]H. Zhang, Q. Zhang, X. Zhao, X. Li, D. Wang, and H. Luo, Appl. Phys. Lett. **102**, 202904 (2013).
[31]M. Zeng, S. W. Or, and H. L. W. Chan, J. Appl. Phys. **107**, 043513 (2010).
[32]H. W. Eng, P. W. Barnes, B. M. Auer, and P. M. Woodward, J. Solid State Chem. **175**, 94–109 (2003).
[33]T. Qi, I. Grinberg, and A. M. Rappe, "Band-gap engineering via local environment in complex oxides," Phys. Rev. B **83**, 224108 (2011).
[34]F. Wang, I. Grinberg, and A. M. Rappe, Appl. Phys. Lett. **104**, 152903 (2014).
[35]B. N. Rao, M. Avdeev, B. Kennedy, and R. Ranjan, Phys. Rev. B **92**, 214107 (2015).
[36]H. D. Megaw and C. N. W. Darlington, Acta Cryst. B **31**, 161–173 (1975).
[37]M. Hinterstein, M. Knapp, M. Hölzel, W. Jo, A. Cervellino, H. Ehrenbergb, and H. Fuess, J. Appl. Cryst. **43**, 1314–1321 (2010).
[38]J. L. Jones and M. Hoffman, Appl. Phys. Lett. **89**, 092901 (2006).

Published under license by AIP Publishing.